The 2020 Monte Cristo (Nevada) Earthquake Sequence: Stress Transfer in the Context of Conjugate Strike-Slip Faults

Jugurtha Kariche

▶ **To cite this version:**

Jugurtha Kariche. The 2020 Monte Cristo (Nevada) Earthquake Sequence: Stress Transfer in the Context of Conjugate Strike-Slip Faults. Tectonics, 2022, 41 (3), 10.1029/2020tc006506 . insu-04470946

HAL Id: insu-04470946

https://insu.hal.science/insu-04470946v1

Submitted on 21 Feb 2024

HAL is a multi-disciplinary open access archive for the deposit and dissemination of scientific research documents, whether they are published or not. The documents may come from teaching and research institutions in France or abroad, or from public or private research centers.

L'archive ouverte pluridisciplinaire **HAL**, est destinée au dépôt et à la diffusion de documents scientifiques de niveau recherche, publiés ou non, émanant des établissements d'enseignement et de recherche français ou étrangers, des laboratoires publics ou privés.

Copyright

Check for updates

Tectonics®

RESEARCH ARTICLE
10.1029/2020TC006506

Key Points:

- The 2020 Monte Cristo earthquake (Mw 6.5) suggests a fault interaction in the context of conjugate strike slip faults
- The Coulomb modeling show no evidence of fluid redistribution related to earthquakes that occurred in the Central Walker Lane
- The reactivation of large active faults in the Southern Walker Lane implies a pore-fluid physical effect

Supporting Information:

Supporting Information may be found in the online version of this article.

Correspondence to:

J. Kariche,
jkariche@usthb.dz

Citation:

Kariche, J. (2022). The 2020 Monte Cristo (Nevada) earthquake sequence: Stress transfer in the context of conjugate strike-slip faults. *Tectonics*, *41*, e2020TC006506. https://doi.org/10.1029/2020TC006506

Received 1 SEP 2020
Accepted 30 JAN 2022

© 2022. American Geophysical Union. All Rights Reserved.

The 2020 Monte Cristo (Nevada) Earthquake Sequence: Stress Transfer in the Context of Conjugate Strike-Slip Faults

Jugurtha Kariche[1,2]

[1]Institut Terre et Environnement de Strasbourg, Université de Strasbourg, UMR 7063 CNRS, Strasbourg, France, [2]Now at USTHB, Laboratoire de Géophysique, FSTGAT, Algiers, Algeria

Abstract On 15 May 2020 at 11:03 (UTC) a shallow earthquake with a Magnitude Mw 6.5 struck the Central Walker Lane in the Mina Deflection region. This shallow event offers the possibility to model the change in Coulomb failure function (ΔCFF) including the historical events and to analyze the effect of fluid redistribution on fault ruptures. The static stress change modeling shows that the 1932 Cedar Mountain (Mw 7.1) earthquake increased ΔCFF on the 2020 Monte Cristo left-lateral rupture by an average value of ∼2 bar suggesting a fault interaction in the context of conjugate strike-slip faults. Also, the ΔCFF caused by the Monte Cristo earthquake shows a 0.1–0.5 bar increase on nearby right-lateral fault planes at 8 km depth. In contrast to the 2019 Ridgecrest sequence (Mw 6.4 and Mw 7.1), our poroelastic stress change modeling of the 2020 Monte Cristo earthquake shows no apparent correlation between the positive stress change values and fluid redistribution along the Monte Cristo conjugated ruptures. Nevertheless, the Coulomb modeling using adapted poroelastic solutions shows that the 2020 Monte Cristo mainshock increased stresses with a value of 0.2–0.9 bar south of the Mina Deflection along the White Mountains and Fish Lake Valley fault zones. The stress values combined with a strain rate of 40–50 nanostrain/yr represent a shift of 8%–15% of the recurrence time interval for a large earthquake along the White Mountains and Fish Lake Valley faults suggesting an elevated pore-fluid effect for faults reactivation in both undrained and drained fluid conditions.

1. Introduction

A significant earthquake occurred on 15 May 2020 (Mw 6.5) in the Monte Cristo Range located in the west part of the Basin and Range province near Tonopah, (Nevada), USA. This event is the strongest earthquake to have occurred in the state of Nevada since 1954, but due to its remote location far from populated areas, no serious damage was reported (Koehler et al., 2021). The earthquake occurred along the eastward projection of the left-lateral Candelaria fault (Koehler et al., 2021; Figure 1).

Aftershock distribution and focal mechanism solutions (Ruhl et al., 2021; Figure 1), surface rupture mapping (Koehler et al., 2021), GPS measurement (Hammond et al., 2021), and surface deformation deduced from Synthetic Aperture Radar Interferogram (InSAR), indicates that the 2020 Monte Cristo event occurred within two distinct zone of seismicity from west to east characterized by a complex pattern of surface rupture between NE-striking oblique left-normal faults, with minor slip on north-striking right-lateral faults. Seismicity and geodesy show a predominantly E-W rupture plane with hints of perpendicular intersecting structures. The tectonic and geomorphologic investigations indicate that the expression of the left-lateral displacement along the 2020 Mw 6.5 Monte Cristo main traces is analogous to the pattern of surface rupture observed in the 2019 Mw 6.4 Ridgecrest earthquake (Koehler et al., 2021). The moment tensor solution and the aftershocks distribution of the Monte Cristo earthquake along the left-lateral Candelaria Hills fault is oriented at a relatively high angle to the general trend of the Walker Lane with respect to the opposite sense of slip (Figure 1), similar to the orientation of the Mw 6.4 Ridgecrest earthquake. Taking into account both seismological and tectonic aspects (Figure 1; Koehler et al., 2021), the left-lateral structure associated with the Monte Cristo earthquake may reflect the primary mechanism whereby the slip is transferred across major right-lateral faults and may imply a stress redistribution due to the fault interactions between neighboring conjugate fault structures as observed in other case studies (Hudnut et al., 1989; Kariche et al., 2018).

In this paper, we investigate the 2020 Monte Cristo seismic sequence and examine potential fault interactions using Coulomb modeling on fixed fault planes derived from field investigations, geodetic and seismic source analysis. The computation using historical events is considered in order to better understand the large-scale fault

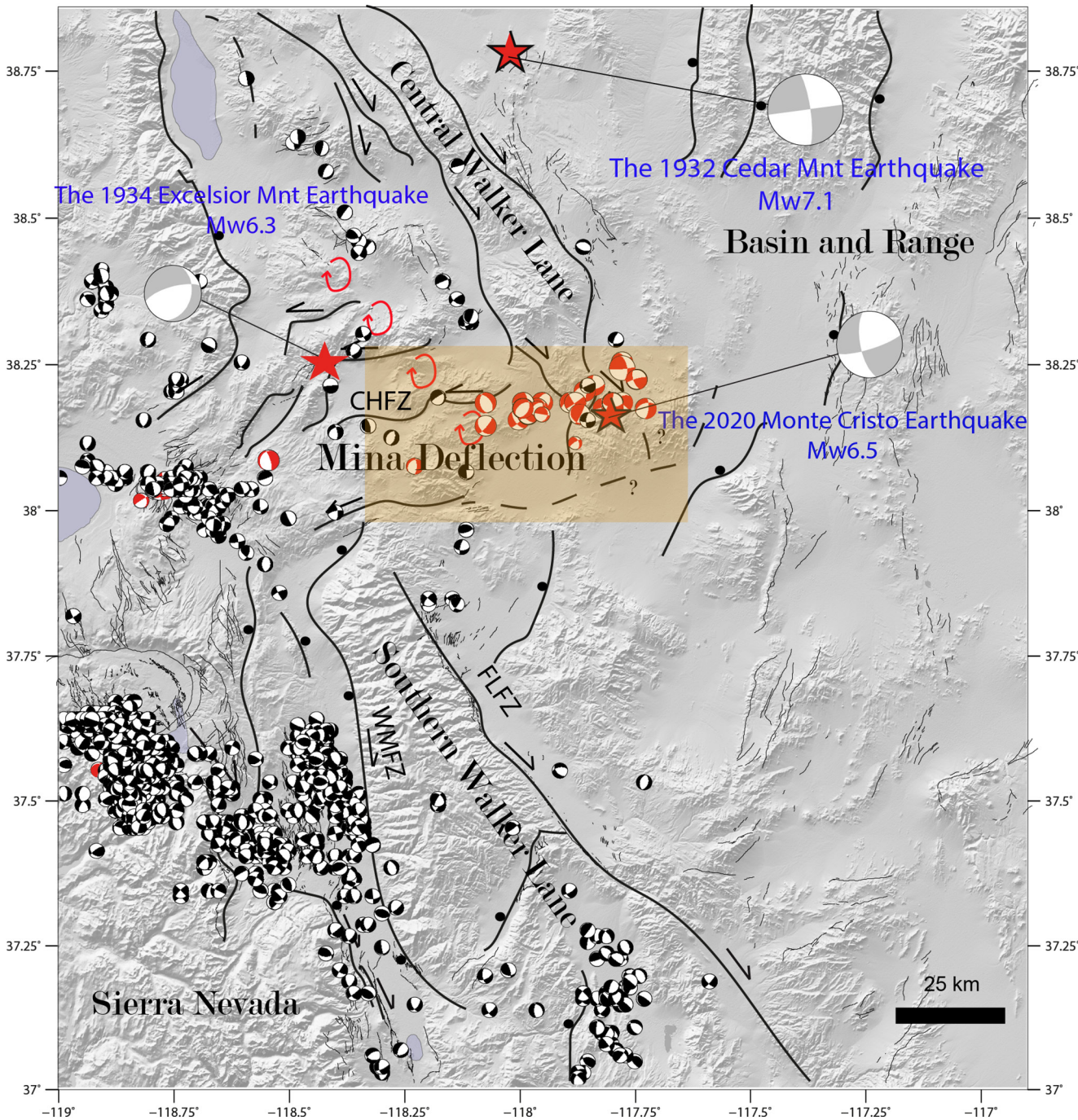

Figure 1. Seismotectonic map showing major active faults of the Walker Lane and Mina Deflection (thick black lines; Wesnousky, 2005). The thin lines represent additional USGS/CGS Quaternary active faults (https://earthquake.usgs.gov/hazards/qfaults/, last updated in 2017). The seismicity ($M > 3$) spanning the period from 1968 to 26/06/2020 are from Northern California Earthquake Catalog, the related focal mechanism is represented with black beach ball. The focal mechanism of the 1932 Cedar Mountains and the 1934 Excelsior Mountain earthquakes are extracted from Doser (1988). The focal mechanism for the Mw6.5 Monte Cristo earthquake is from USGS-NEIC (https://earthquake.usgs.gov/earthquakes/search/). The red beach balls represent the 2020 Monte Cristo earthquake aftershocks moment tensor solutions. The red beach balls data are from Saint Louis University (SLU). The colored Box indicates the 2020 Monte Cristo sequence. CHFZ= Candelarias Hills Fault zone; FLFZ= Fish Lake Valley Fault zone; WMFZ= White Mountains Fault zone. The clockwise block rotation (Wesnousky, 2005) is indicated by red arrows.

interaction and related fluid migration. The Coulomb modeling shows a stress transfer from large right-lateral fault ruptures to nearby major left-lateral conjugate fault ruptures. Using different values of the effective friction coefficient closely connected to variable Skempton coefficient values, the stress change modeling suggests

19449194, 2022, 3, Downloaded from https://agupubs.onlinelibrary.wiley.com/doi/10.1029/2020TC006506 by Portail BibCNRS INSU, Wiley Online Library on [21/02/2024]. See the Terms and Conditions (https://onlinelibrary.wiley.com/terms-and-conditions) on Wiley Online Library for rules of use; OA articles are governed by the applicable Creative Commons License

different pore pressure regimes along different faults within the Walker Lane. Also, the Coulomb stress modeling shows that the ∼3-month aftershocks distribution following the 2020 Monte Cristo earthquake is driven by a stress transfer. The Coulomb modeling results related to the 2020 Monte Cristo earthquake sequence are also compared to the stress transfer following the 2019 Ridgecrest earthquake sequence. The effect of pore-fluid in the triggering mechanism for both sequences (i.e., 2020 Monte Cristo and 2019 Ridgecrest) and the occurrence of liquefaction are also discussed.

2. Seismotectonics and Fault Parameters

The seismicity in the Walker Lane and Mina Deflection is due to the relative movement of the Pacific & North American plates. Global positioning system (GPS) measurements indicate that the Walker Lane accommodates 15%–25% of the dextral motion between the North American and Pacific plates from north to south (Bennett et al., 2003; Blewitt et al., 2018; Hammond et al., 2021; Thatcher et al., 1999; Wesnousky, 2005). The Walker Lane is divided in terms of the complexity of the pattern of faulting and block rotations into three distinct structural domains defined by different *physiographic expression and style of deformation* (Faulds et al., 2005; Wesnousky, 2005). The Northern Walker Lane consists of a system of faults that have variable orientations (Wesnousky, 2005). The north-northwest trending right-lateral strike-slip faults are associated with clockwise crustal blocks rotations bounded by deep-seated, high angle normal faults, left-lateral strike-slip faults, and right-lateral strike-slip faults (Carlson et al., 2013; Faulds et al., 2005; Wesnousky, 2005). Paleoseismic and geomorphic studies indicate Holocene slip rate ranging from 1.1 to 2.6 mm/yr (Carlson et al., 2013; Faulds et al., 2005; Wesnousky, 2005). The Southern Walker Lane is tectonically more mature and better organized and extends from the Garlock fault to the Mina Deflection (Faulds et al., 2005; Wesnousky, 2005). It consists of continuous ∼ hundreds of kilometers long northwest-trending right-lateral fault systems. The 250-km long NW striking Fish Lake Valley-Death Valley fault zone is the longest fault system that composes the Southern Walker Lane (Wesnousky, 2005). The fault slip rate along the Fish Lake Faults Valley-Death Valley fault system averages ∼3.3 mm/yr (Wesnousky, 2005). Other major dextral faults that encompass the Southern Walker Lane are the Owens-Valley-White Mountains faults. This system of faults is characterized by a slip rate of ∼2.9 mm/yr on the Owens Valley fault partitioned essentially onto the NNW White Mountain fault zone (DeLano et al., 2019). The two separate but northward converging fault systems migrate from Fish Lake Valley to the White Mountains and Owens Valley faults along northeast striking normal faults (Carlson et al., 2013; Wesnousky, 2005; Figure 1). Geodetic data indicate that more than 10 mm/yr of dextral shear is associated to the Southern Walker Lane domain (Bormann et al., 2016; Kreemer et al., 2009).

The Central Walker Lane is characterized by heterogeneous and discontinuous systems of NW striking right-lateral faults, NE striking conjugate left-lateral faults, and N striking normal faults denoting a significant change in the style of deformation between the Northern and the Southern Walker Lane (Angster et al., 2019; Carlson et al., 2013; Wesnousky, 2005). A maximum long-term geological dextral fault slip rate of ∼1.5 mm/yr deduced from displaced Holocene alluvial fan deposits is accommodated along to the Benton Spring Fault zone (Angster et al., 2019).

Faulds et al. (2005) defines the Central Walker Lane as the youngest parts of the transform plate boundary system which accommodates a significant fraction of the Pacific-North American plate motion. Kinematic modeling, paleomagnetic results and seismicity analysis show that the Central Walker Lane is associated with a three domains that accommodate the complex active deformation (Bormann et al., 2016, Figure 1): (a) left-lateral faulting with a clockwise (Non Pinned) block rotation upon a vertical axis from the Excelsior Mountains to Candelaria Hills within the Mina Deflection; (b) right-lateral faulting to the northeast and southwest of the Mina deflection: and (c) extensional faulting with a probable clockwise block rotation and related *en-echelon* normal faulting pattern from the Mina Deflection to the Southern Walker Lane. Several authors interpret this complex rotational domain as the major mechanism controlling the dynamics of extensional basins within the Walker Lane (Angster et al., 2019; Bormann et al., 2016; Nagorsen-Rinke et al., 2013; Pierce et al., 2021; Wesnousky, 2005). Faulds et al. (2005) interpret the complex kinematics domain as a consequence of the early evolution of a strike slip faults systems in both a transtensive and transpressive regimes and infer that this pattern may denote the birth of a new lithospheric-scale transform fault.

19449194, 2022, 3, Downloaded from https://agupubs.onlinelibrary.wiley.com/doi/10.1029/2020TC006506 by Portail BibCNRS INSU, Wiley Online Library on [21/02/2024]. See the Terms and Conditions (https://onlinelibrary.wiley.com/terms-and-conditions) on Wiley Online Library for rules of use; OA articles are governed by the applicable Creative Commons License

19449194, 2022, 3, Downloaded from https://agupubs.onlinelibrary.wiley.com/doi/10.1029/2020TC006506 by Portail BibCNRS INSU, Wiley Online Library on [21/02/2024]. See the Terms and Conditions (https://onlinelibrary.wiley.com/terms-and-conditions) on Wiley Online Library for rules of use; OA articles are governed by the applicable Creative Commons License

Table 1
Physical Characteristic of the Earthquakes Used in This Study, L Represent the Fault Length and W is Fault Width

Earthquake	Lon_c (°)	Lat_c (°)	Depth (km)	M_O ($\times 10^{18}$ N.m)	L (km)	W (km)	Strike (°)	Dip (°)	Reverse slip (m)	Right-lateral Slip (m)
1932 Cedar Mnt	−117.9	38.6	7.5	44	49.60	15.23	347	80	0.000	1.8
1934 Excelsior Mnt	−118.35	38.28	5.5	3.7	22	13	246	45	−0.1	−0.4
2020 Monte Cristo	−117.81	38.23	4.0	0.2	13.8	5.1	158	82	−0.01	[1]0.1
	−177.89	38.16	9.0	2.9	20	15.3	73	78	−0.12	−0.28
	−118.03	38.12	5.7	2.8	10	11	56	50	−0.54	−0.59

Note. Lon_c and Lat_c indicates the center of each dislocation.

Figure 1 represents a seismotectonic map of the Central Walker Lane domain. The largest historical event in the Central Walker Lane, the 1932 Cedar Mountain earthquake occurred near the Cedar Mountains with a magnitude Mw 7.1 (Doser, 1988, Figure 1). The focal solution combined with field observations show that this event occurred on a complex system of right-lateral faults (Bell et al., 1999; Doser, 1988; Figure 1). The waveform inversion and other seismic considerations show that the rupture process of the Cedar Mountain earthquake initiated at the northeastern edge of the Central Walker Lane and propagated southward for about 10 s (Doser, 1988). By analyzing the focal solution of the 1932 Cedar Mountain event, Doser (1988) inferred that the nodal plane with a strike/dip/rake = 352°/80°/180° matches the principal trend of the Cedar Mountain rupture. Based on analyses of focal solutions and the extent of the damage zone as reported by Bell et al. (1999), the Cedar Mountain fault parameters show a ∼60-km-long, ∼15-km-wide north-north-east south-south-west trending zone of strike slip faults associated with 1.5 ± 0.3 m right-lateral slip. The seismic moment obtained using the Wells and Coppersmith (1994) empirical relations show a $M_0 \sim 4.4 \times 10^{19}$ N.m (Table 1) in agreement with the $\sim 5.4 \times 10^{19}$ N.m geologic moment estimate of Doser (1988).

Another major earthquake that occurred in the Central Walker Lane is the 30 January 1934 Excelsior Mountain earthquake with magnitude of Mw 6.3 (Doser, 1988; Ryall & Priestley, 1975). Focal mechanism analysis, aftershock relocation and tectonic considerations indicate that this event occurred on a conjugate left-lateral fault with respect to the 1932 Cedar mainshock (Table 1, Figure 1). The aftershock distribution following the 1934 Excelsior Mountain Earthquake shows that this event was followed by more than 30 aftershocks with Magnitude ≥4.0 (Ryall & Priestley, 1975). The spatial distribution of aftershocks implies that the 1934 Excelsior Mountain earthquake occurred along a fault plane striking between N49°E and N60°E and dipping between 40°NW to 70°NW (Bell et al., 1999; Doser, 1988).

The 2020 Mw 6.5 Monte Cristo Range earthquake has been the site of numerous published studies as of the time of this writing with extensive documentation on earthquake rupture, aftershock distribution and surface faulting (Bormann et al., 2021; Hammond et al., 2021; Koehler et al., 2021; Ruhl et al., 2021). A precise relocation of ∼17,000 events, moment tensor solutions, and the rapid tectonic-geomorphic reconnaissance demonstrate that the 2020 Monte Cristo earthquake occurred at the intersection of two distinct fault zones characterized by a ∼30 km E-NE zone of complex fault-ruptures with variable senses of slip that accommodate overall East-West left-lateral shear deformation (Bormann et al., 2021; Koehler et al., 2021; Ruhl et al., 2021). The Western zone is characterized by a wide area of damage characterized by a predominantly left-lateral offsets with a right-stepping *en echelon* fault-rupture geometries (Koehler et al., 2021; Ruhl et al., 2021) comparable to those observed during the 2019 (Mw 6.4) Ridgecrest earthquake (Ponti et al., 2020). Surface rupture investigations show a maximum of ∼20 cm left-lateral displacement measured from an offset channel margin and 10 cm of NW vertical displacement, indicating a component of oblique slip (Koehler et al., 2021). The Eastern zone of the rupture including the location of the 2020 Monte Cristo mainshock is quite different. The spatial evolution of seismicity and aftershocks moment tensor solutions shows a more complex distribution of faults with a cluster of events aligned N to NW associated with predominantly right-lateral slip (Ruhl et al., 2021) comparable to the surface rupture mapping observations (Koehler et al., 2021). The seismicity near the hypocenter is concentrated on shallow oblique structures with ranging in depth between [3–10] km (Ruhl et al., 2021).

As mentioned before, focal mechanisms combined with the analysis of aftershocks distribution, GPS and InSAR data show that the 2020 Monte Cristo earthquake occurred on complex E-W predominantly left-lateral faults

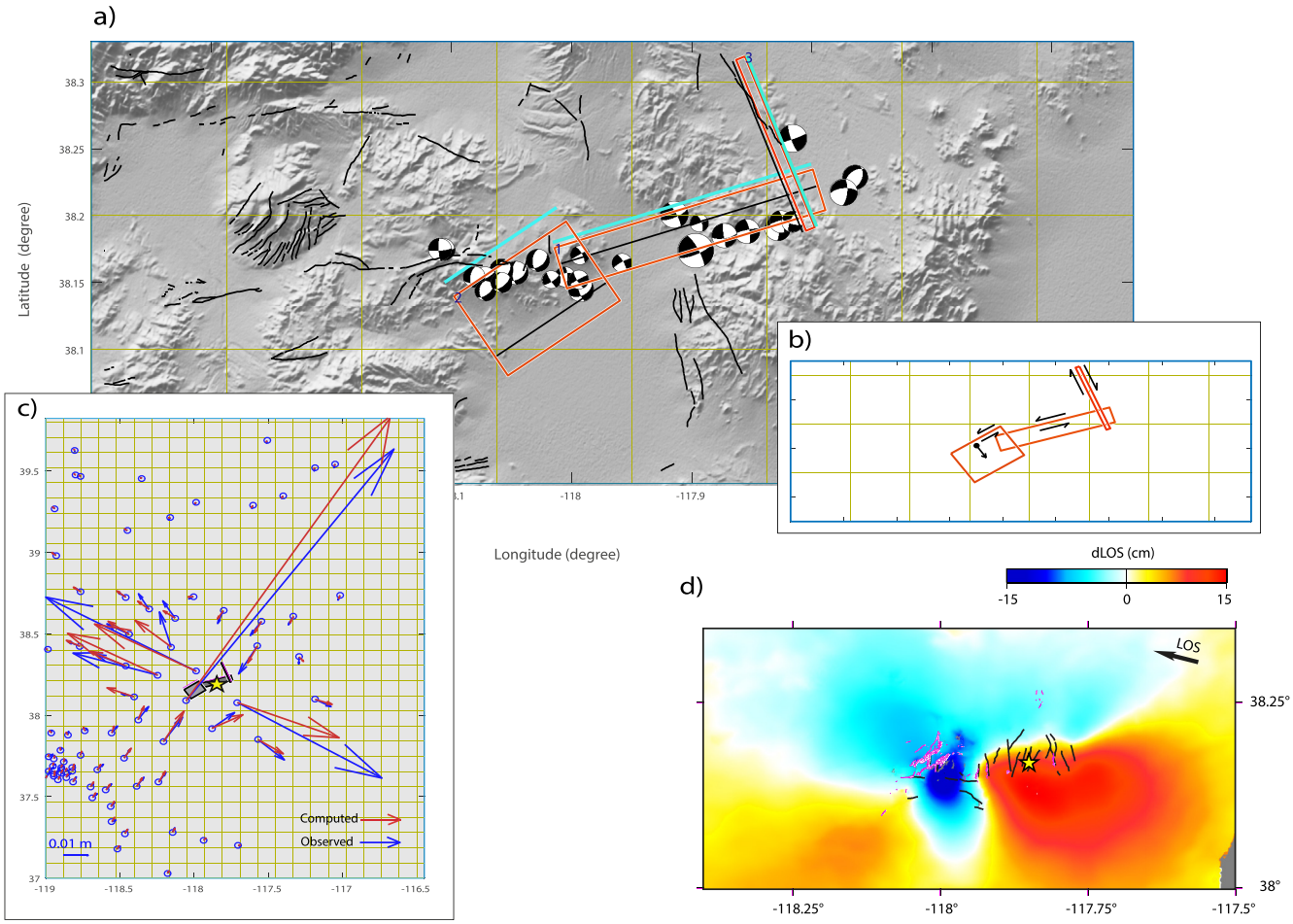

Figure 2. Preferred fault geometry and slip distribution related to the 2020 Monte Cristo earthquake (Mw 6.5) and used as an input to the Coulomb stress change modeling: (a) Correspondence between focal solutions for major events ($M \geq 4$) associated with the 2020 MC sequence and our estimated fault geometry used as an input to the Coulomb modeling, the rectangles indicate the projection of fault planes at the surface and the magenta lines indicate the fault trace. The black lines represent the Quaternary faults. (b) General slip distribution following the Mw 6.5 Monte Cristo earthquake, the arrows represent the sense of slip. (c) Comparison between the modeling coseismic displacement (in red) and the observed coseismic GPS displacement (in blue). The updated coseismic offsets data are from MAGNET/UNAVCO-NOTA real time data solutions. (d) Coseismic InSAR line-of-sight (LOS) displacement derived from Sentinel-1A interferograms (data from Li et al., 2020). The Sentinel data used to retrieve the coseismic LOS displacement is acquired in the Descending Tracks 144, the black lines represent the InSAR estimation of the 2020 Monte Cristo fractures network (R.Gold pers. comm.) and the purple surface represent the surface ruptures obtained by Koehler et al. (2021) and Dee et al. (2021). Yellow star indicates earthquake epicenter. The comparison between modeled and observed displacements is performed using the Coulomb 3.3 software (Toda et al., 2011).

(Table 1, Figure 2; Koehler et al., 2021; Ruhl et al., 2021). In the context of a dextral movement along the Pacific -North American plate boundary system, the E-W Monte Cristo earthquake rupture and related shallow seismicity can be interpreted as transtension deformation accommodating a clockwise block rotation upon a vertical axis which is characteristic of movement of major conjugate strike-slip faults in the Central Walker Lane (Figure 1; Wesnousky, 2005). Using the empirical relations from Wells and Coppersmith (1994), the magnitude of the 2020 Monte Cristo event implies 0.6 m coseismic left-lateral slip at depth and ~20-km complex-wide rupture (Table 1, Figure 2) consistent with the GPS data and geological field investigations (Hammond et al., 2021; Koehler et al., 2021). The Monte Cristo slip model proposed in this study (Table 1) also mimics the change in orientation and sense of slip as observed in GPS data, seismicity analysis, and field investigations (Hammond et al., 2021; Koehler et al., 2021; Ruhl et al., 2021).

19449194, 2022, 3, Downloaded from https://agupubs.onlinelibrary.wiley.com/doi/10.1029/2020TC006506 by Portail BibCNRS INSU, Wiley Online Library on [21/02/2024]. See the Terms and Conditions (https://onlinelibrary.wiley.com/terms-and-conditions) on Wiley Online Library for rules of use; OA articles are governed by the applicable Creative Commons License

19449194, 2022, 3, Downloaded from https://agupubs.onlinelibrary.wiley.com/doi/10.1029/2020TC006506 by Portail BibCNRS INSU, Wiley Online Library on [21/02/2024]. See the Terms and Conditions (https://onlinelibrary.wiley.com/terms-and-conditions) on Wiley Online Library for rules of use; OA articles are governed by the applicable Creative Commons License

3. Stress Change Modeling and Fault Interaction

3.1. Coseismic Stress Change Response

To evaluate potential fault interactions caused by major earthquakes on nearby fault ruptures, we use the concept of change in Coulomb Failure Function (ΔCFF). The static stress change can be expressed by (Reasenberg & Simpson, 1992):

$$\Delta\text{CFF} = \Delta\tau - \mu'\Delta\sigma n; \quad (1)$$

In which τ is the shear stress, σn is the normal stress, μ′ is the effective friction coefficient and ′ refers to changes during an earthquake. The apparent (or effective) friction coefficient μ′ can be expressed as the combination of Skempton coefficient B and internal friction coefficient μ (Reasenberg & Simpson, 1992):

$$\mu' = \mu(1 - B) \quad (2)$$

[1]The preferred dislocation model for the 2020 Monte Cristo earthquake consists of the combination of three conjugate segments with a mixed right-lateral, left-lateral (primarily) and normal slip components. Note that the faults geometry and slip distributions agree with the GPS, InSAR line-of-sight (LOS) displacements and focal solutions of major aftershocks (see Section 4 and Figure 2 for more details).

Based on the isotropic poroelastic hypothesis, an expression of the Coulomb stress change is given by (Beeler et al., 2000):

$$\Delta\text{CFF} = \Delta\tau - \mu(\Delta\sigma n - B\Delta\sigma m) \quad (3)$$

where Δσm defines the mean stress change following the earthquake. In this work, the concept of the isotropic poroelastic medium as expressed by Beeler et al. (2000) is compared to the classic elastic Coulomb stress change modeling to assess the effect of pore fluid pressure change on earthquake triggering mechanisms on conjugate faults. The ΔCFF computation is resolved on known fixed fault planes deduced from: focal mechanism data, InSAR and GPS data analysis, strong wave motion inversion and other geological considerations (Table 1, Figures 1 and 2).

3.2. Short Term Postseismic Poroelastic Stress Response

At the intermediate between undrained and drained fluid phases, the Skempton coefficient B may be related to the undrained and drained state of fluids as (Yamashita & Tsutsumi, 2018):

$$\frac{K}{K_u} = 1 - \alpha B$$

where α is called as the Biot and Willis coefficient (1957) and represents the ratio between the increment fluid content and the volumetric strain change following an earthquake. K and K_u represent the drained and undrained bulk modulus respectively and may be written as a contribution of undrained (υ_u) and drained (υ) Poisson ratios (Yamashita & Tsutsumi, 2018):

$$\frac{K}{K_u} = \left(\frac{1+\upsilon}{1+\upsilon_u}\right) \times \frac{\upsilon_u}{\upsilon}$$

If an isotropic poroelastic model is assumed (Beeler et al., 2000), an intermediate short-term poroelastic solution can be obtained by combining a shear, normal and pore fluid contribution as:

$$\Delta\text{CFF} = \Delta\tau - \mu(\Delta\sigma n - \frac{(\upsilon_u - \upsilon)}{\alpha\ (1-2\upsilon)(1+\upsilon_u)}\Delta\sigma_{kk}) \quad (4)$$

Equation 4 shows that the effect of pore fluid is not a maximum in the undrained phase of fluids but a significant pore fluid perturbation may appear from the undrained to the drained fluids-phase. This approach is also examined by Segall and Rice (1995) and Chambon and Rudnicki (2001) in stress change induced by fault geometries in a spring-slider model for dilating fluid-infiltrated fault. Equation 4 represents the short-term coupled poroelastic

response of the medium following a sudden slip. Comparing Equations 1 and 4 and considering partially saturated conditions in rocks in the upper few kilometers of the seismogenic zone ($h \leq$ 15-km depth) with typical values of $(\upsilon_u, \upsilon) = 0.31, 0.25$ (Bosl & Nur, 2002; Rice & Cleary, 1976), then the coupled poroelastic stress change response on fixed fault ruptures shows a value ~10% greater than the ΔCFF values obtained by elastic stress change modeling (Equation 1). These typical values of υ_u and υ correspond to the case where the elastic properties of crustal rocks are affected by the presence of fluids. These values also describe the temporal change in the ratio of the compressional and shear wave velocities (V_p/V_s) following an earthquake.

Considering a high density of pre-existing fractures associated with fully saturated rocks ($\upsilon_u, \upsilon = 0.31, 0.15$), the average poroelastic stress response on target faults is ~40% greater than the Coulomb stress modeling using only the elastic properties of the upper crust. Based on this assumption and considering the presence of fluids along the fault zone, the short-term coupled poroelastic response tends to increase the stress loading on fixed receiver faults in locations where the fluid diffusion cause increases in pore-fluid pressure over time.

3.3. Intermediate to Long Term Postseismic Poroelastic Stress Response

The absence of a real 3D poroelastic model inhibits the physical characterization of the complex fluid diffusion process along active faults. To overcome this limitation, the cumulative stress change associated with the full poroelastic relaxation of an earthquake is modeled by adopting analytical 3D poroelastic solutions based on 3D elastic modeling. This modeling accounts for the temporal variation of the Poisson ratio from undrained to the fully drained state of fluids. The modeling approach is not necessarily viewed as an oversimplified assumption. The strategy adopted here is based on comparing elastic deformation scenarios from the "undrained "state of the fluid (i.e., immediately after the earthquake) to the possible fully "drained "fluid state (i.e., when the fluid is fully redistributed and heterogeneous fluid pressure state has been re-established along the fault zone) but without exploring the details in the temporal evolution of the fluid migration and crustal deformation. In this case, the variation of the Poisson ratio from undrained to drained fluid state is viewed as a consequence of the variation in rock rheology due to the fluid drainage along the fault zone. This basic approach is also adopted by Peltzer et al. (1998) to invert post-seismic deformation due to the poroelastic rebound of major earthquakes in Southern California.

4. Earthquake Sequence and Static Stress Change in the Central Walker Lane

The seismicity catalog within the Walker Lane tectonic province includes recorded historical seismicity and pre-instrumental observations indicates the occurrence of numerous Mw > 6 earthquakes (Figure 1). This activity mostly shows a conjugate right-lateral and left-lateral rupture mechanisms within the Central Walker Lane (Figure 1). This sequence of seismic activity suggests stress transfer among of conjugate faults as observed in other cases such as the November 1987 Elmore Ranch-Superstitions Hills, the 1992 Landers-Big Bear, the 1994–2016 Rif-Alboran Sea, the 2019 Mindanao and the July 2019 Ridgecrest earthquakes sequences (Bosl & Nur, 2002; Hudnut et al., 1989; Kariche et al., 2018, 2019; Li et al., 2020). Fault slip kinematic studies for the Walker Lane and Mina Deflection show a slip transfer between sinistral slip along the northwest part of the Mina Deflection and dextral slip along the Owens Valley fault in the Southern Walker Lane domain (DeLano et al., 2019; Nagorsen-Rinke et al., 2013; Stewart, 1980; Wesnousky, 2005). In the context of lateral movement along the Pacific-North American transform plate boundary, *en echelon* left-lateral faults delimited by large dextral faults can be interpreted as a transpression/transtension deformation with a clockwise block rotation (Jackson & Molnar, 1990). Kinematic modeling with clockwise vertical axis block rotation and paleomagnetic results illustrate pure shear crustal deformation oriented approximatively parallel to the Walker Lane (Jackson & Molnar, 1990; Wesnousky, 2005). Wesnousky (2005) points out that the clockwise rotation of crustal blocks appears responsible for major basins within the Central Walker Lane.

The seismic sequences investigated in this study includes the three strong to major earthquakes that occurred in the Central Walker Lane–Mina Deflection (Figure 1): The 1932 Cedar Mountain earthquake (Mw 7.2), the 1934 Excelsior Mountain earthquake (Mw 6.3) and the 2020 Monte Cristo Range earthquake (Mw 6.5). The Cedar Mountain and Excelsoir Mountain events have been the focus of geomorphologic and tectonic investigations and seismic waveform analyses (Doser, 1988; Ryall & Priestley, 1975; Wesnousky, 2005) from which the epicentral

19449194, 2022, 3, Downloaded from https://agupubs.onlinelibrary.wiley.com/doi/10.1029/2020TC006506 by Portail BibCNRS INSU, Wiley Online Library on [21/02/2024]. See the Terms and Conditions (https://onlinelibrary.wiley.com/terms-and-conditions) on Wiley Online Library for rules of use; OA articles are governed by the applicable Creative Commons License

19449194, 2022, 3, Downloaded from https://agupubs.onlinelibrary.wiley.com/doi/10.1029/2020TC006506 by Portail BibCNRS INSU, Wiley Online Library on [21/02/2024]. See the Terms and Conditions (https://onlinelibrary.wiley.com/terms-and-conditions) on Wiley Online Library for rules of use; OA articles are governed by the applicable Creative Commons License

locations and related fault-rupture characteristics are derived (Table 1). The fault rupture geometry and parameters associated with the 2020 Monte Cristo earthquake are deduced from modeling of coseismic offset on 24 MAGNET GPS stations, SLU focal mechanisms, source time functions and co-seismic Sentinel-1A InSAR data analysis (Figure 2). Based on elastic dislocation theory (Okada, 1992), our preferred model constrained by GPS, InSAR and moment tensor solutions data consists of a combination of three conjugate segments with a mixed right-lateral, left-lateral and normal slip distributions (Table 1, Figure 2). The spatial variability of the geometry and the slip distributions from E to W derived from this model align with the spatial evolution of aftershocks and surface ruptures investigations (Koehler et al., 2021; Ruhl et al., 2021).

Among the largest earthquakes (Mw > 6) to have occurred in the Central Walker Lane, the 1932 Cedar Mountain (Mw 7.1), the 1934 Excelsior Mountain (Mw 6.3) and the 2020 Monte Cristo (Mw 6.5) seismic sequences suggest a southward migrating pattern of seismicity (Figures 3a–3c). In comparison with the stress transfer controlled by *en echelon* thrust faults related to the transpressive regime with a clockwise "pinned" block rotation that characterizes the oblique convergence in the western Mediterranean region (Kariche et al., 2017), the earthquake activity in the Central Walker Lane appears to be controlled by a set of conjugate strike slip faults. The seismotectonic analysis shows a clear distinction between moderate size-earthquakes that occurred along the *en echelon* ENE-WSW sinistral strike slip faults and large earthquakes that occurred along NNW-SSE dextral strike slip faults that are conjugate to them (Figure 1). Figure 3 shows that the southeastward to southward earthquake migration in the Central Walker Lane is partially due to the fault interaction and related stress transfer. The static stress change modeling shows that the 1932 Cedar Mountain earthquake affects the stress distribution on both the 1934 Excelsior Mountain and 2020 Monte Cristo earthquake source areas. The stress redistribution following the 1932 Cedar Mountain earthquake shows an increase ΔCFF on the Excelsior Mountain fault rupture with values >0.1 bar (see Table 2 and Figure 3a).

The Coulomb stress transfer hypothesis may be viewed as a mechanism explaining the time delay between earthquakes, if we assume a population of faults at different stages of their seismic cycle with similar geological slip rates (Figure 4a). The positive stress change value should alter the earthquake recurrence interval on these faults by the linear equation (Stein et al., 1997):

$$Tr' = Tr - \Delta CFF/\dot{\tau} \tag{5}$$

where Tr' is the calculated recurrence time, Tr is the mean recurrence time before the earthquake, $\dot{\tau}$ is the tectonic stressing rate and $\Delta t = \Delta CFF/\dot{\tau}$ is the earthquake clock-time advance. Using the linear elastic stress-strain tensorial approach, the tectonic stressing rate is obtained by assuming that the stress is transmitted elastically in the seismogenic layer (10–15 km thickness). The stressing rate is computed from the strain rate which is derived from the continuous GPS measurement (Kreemer et al., 2014) and compared to the seismic moment rate $\dot{M}$ following the equation:

$$\dot{M} = 2\mu \sum W\dot{\varepsilon}/k \tag{6}$$

where μ is the shear modulus, Σ is the surface area of the region, W is the seismogenic thickness, $\dot{\varepsilon}$ is the strain rate and k is a dimensionless constant that adjusts for the inefficiency of randomly oriented faults to accommodate strain. The value of k is fixed to 1, according to the Kostrov's summation.

Considering an average background stressing rate of ~860 Pa/yr within the Central Walker Lane obtained from: the global tectonic strain rate map (Kreemer et al., 2014), the shallow seismicity, and the stress change imparted by source faults (Table 2, Figure 3), the average value of earthquake clock time advance Δt caused by the 1932 Cedar Mountain earthquake near the hypocentral area of the 1934 Excelsior Mountain earthquake is estimated to be ~60 years. Taking into account the same background stressing rate, the clock time advance caused by the cumulative stress change due to the 1932 Cedar and 1934 Excelsior earthquakes near hypocentral area of the 2020 Monte Cristo event exceed 200 years. This value results from ~2 bar of cumulative stress change imparted by the two historical events.

In contrast to triggering mechanisms in other conjugate earthquake sequences (Hudnut et al., 1989; Kariche et al., 2018), the ΔCFF modeling in the Central Walker Lane shows that the left-lateral fault reactivation does not necessarily require a low effective friction coefficient μ' (Figure 4c). For example, the modeling of static stress

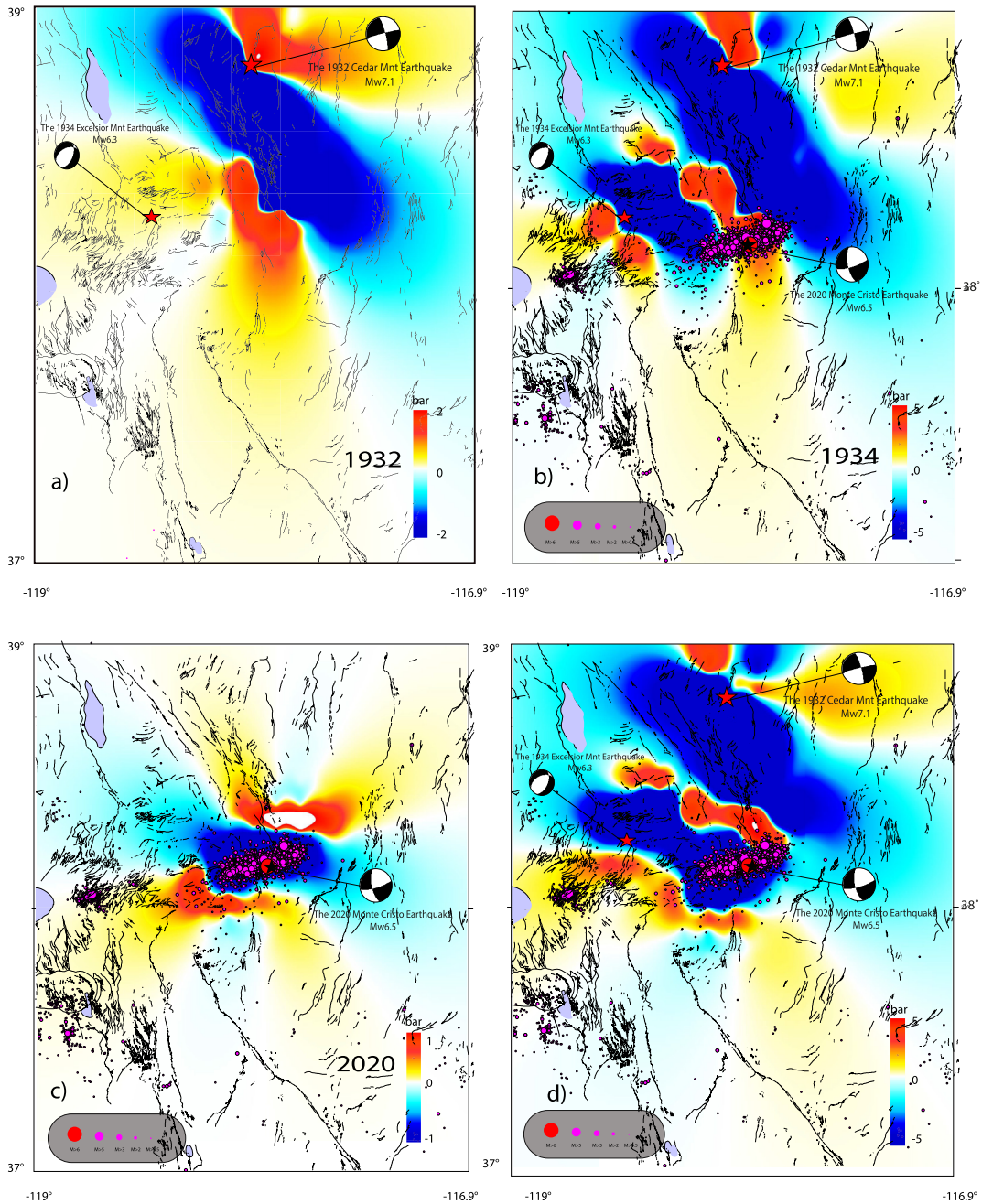

Figure 3. (a) Static stress change ΔCFF caused by the 1932 (Mw 7.1) Cedar Mnt earthquake on fixed fault planes with strike/dip/rake = 228°/45°/-70°, (b) Cumulative ΔCFF caused by the 1932 (Mw 7.1) and the 1934 (Mw 6.3) earthquake sources on fixed fault planes with strike/dip/rake = 73°/78°/-24°, the epicenter locations of source and receiver quakes are represented by red and black stars respectively. (c) Computed ΔCFF caused by the 2020 Monte Cristo earthquake (Mw 6.5) on fixed conjugate right-lateral ruptures with strike/dip/rake = 340°/80°/167°. (d) Computed cumulative ΔCFF with the three earthquakes as a source on fixed conjugate fault planes with strike/dip/rake = 340°/80°/167°, the colored circles represent a ~1 month seismicity following the MC earthquake. The ΔCFF is performed at depth of 8 km with μ' ≥ 0.4 using the Coulomb 3.3 software (Toda et al., 2011). The earthquakes database following the 2020 Monte Cristo earthquake is from USGS-NEIC. The active Quaternary faults are from USGS. The 1932 and 1934 fault ruptures are from Doser (1988).

change caused by the 1932 Cedar Mountain event on the Excelsior Mountain fault rupture implies a high-stress change load when the values of effective friction coefficient μ' exceed 0.4. Comparable results are also obtained on the Monte Cristo fault zone considering both uniform and non-uniform crustal rheologies (Figure 4c; Figures

19449194, 2022, 3, Downloaded from https://agupubs.onlinelibrary.wiley.com/doi/10.1029/2020TC006506 by Portail BibCNRS INSU, Wiley Online Library on [21/02/2024]. See the Terms and Conditions (https://onlinelibrary.wiley.com/terms-and-conditions) on Wiley Online Library for rules of use; OA articles are governed by the applicable Creative Commons License

19449194, 2022, 3, Downloaded from https://agupubs.onlinelibrary.wiley.com/doi/10.1029/2020TC006506 by Portail BibCNRS INSU, Wiley Online Library on [21/02/2024]. See the Terms and Conditions (https://onlinelibrary.wiley.com/terms-and-conditions) on Wiley Online Library for rules of use; OA articles are governed by the applicable Creative Commons License

Table 2
Shear, Normal, and Coulomb Stress Change for Majors Earthquakes Occurred in the Central Walker Lane-Mina Deflection

	Calc. Location			Receiver Faults (°)			Stress computation (bar)		
EQ (SF-RF)	Long (°)	Lat (°)	Z (km)	Strike	Dip	Rake	Shear	Coulomb	Normal
1932 Cedar Mnt (SF) 1934 Excelsior Mnt (RF)	−118.245	38.326	8.00	228	45	−70	0.222	0.217	0.308
1932 Cedar Mnt + 1934 Excelsior Mnt (SF) 2020 Monte Cristo (RF)	−117.882	38.177	8.00	73	78	−24	0.800	2.924	1.970

Note. Fault geometries used in the stress change modeling are defined in Table 1. SF and RF are the source and receiver faults respectively. The Coulomb stress change values on nucleation sites are obtained using the Coulomb 3.3 software with an effective friction coefficient μ' fixed at 0.4.

S1 and S2 in Supporting Information S1). These values suggest that there is no evidence for a significant role of elevated pore fluid pressure near the *en echelon* left-lateral fault systems in the Central Walker Lane- Mina Deflection.

In contrast, the increase in clock time advance from north to south along the *en echelon* left-lateral faults seems to be in good agreement with the observed decrease in clockwise rotations from the north to the south as determined by paleomagnetic and geologic studies (Lee et al., 2009; Petronis et al., 2009; Stewart, 1980). The spatial variation in clock time advance also agrees with the contemporary rotation rates (variation from 1,039 ± 0.179°/M*yr* along the Excelsior block to 0.380 ± 0.161°/M*yr* along the Monte Cristo block) as determined from dense GPS measurements (Bormann et al., 2016). The clock time advance values represent the effect of stress transfer on the earthquake cycle along fault ruptures. The Cedar Mountain, Excelsior Mountain, and Monte Cristo Range conjugated fault ruptures may be seen as a complex mechanical system governed by both fault interaction and rotation of tectonic blocks. This assumption may be generalized to other *en echelon* left-lateral ruptures that compose the Mina Deflection.

The observed increase in clock time advances from north to south Mina Deflection is computed taking into account the entire seismic sequences. For example, the aftershock moment release following the 1932 Cedar Mountains earthquake is added as a source of stress (Figure 4c and Figure S1 in Supporting Information S1). The Coulomb stress modeling based on the entire post-seismic deformation (Figure S1 in Supporting Information S1) shows that the magnitude of stress and related clock time advance on Excelsior and Monte Cristo Range faults are strongly influenced by the variation of shear and normal stress acting on faults rather than elevated pore fluid pressure due to volumetric strain change and/or fluid redistribution along the left-lateral ruptures. The faulting histories within the *en echelon* left-lateral faults that define the Mina Deflection domain appear to be controlled by the geometries of left-lateral faults accommodated essentially by block rotation. The clock time advance values and related positive stress load seem to be largely due to the effect of the frictional properties of rocks. Also, the stress change modeling results using different values of effective friction coefficient (Figures 3a, 3b, and 4c and Figure S1 in Supporting Information S1) support the idea that the slip in active faults is controlled essentially by the kinematics of block rotating (Nur et al., 1986) and fault interactions.

The spatial variation in clockwise rotation suggests a spatial variation in earthquake clock time advance which directly affects the earthquake recurrence time intervals of active faults along the Central Walker Lane. The stress change modeling along the *en echelon* left-lateral faults using different values of effective friction coefficient implies different frictional behaviors along active faults that compose the Mina Deflection tectonic domain. The variation in rotation rates from Excelsior to Monte Cristo blocks combined with the mechanics of fault interactions suggest that the magnitude of distributed shear between faults controls the earthquake recurrence time.

5. The 2020 Monte Cristo Aftershock Sequence, Postseismic Stress Redistribution and Role of Fluids

In this section, I explore the relation between the near field pore pressure change during the 2020 Monte Cristo earthquake sequence and the distribution of the aftershock sequence. Modeling adopted in this study is used as a comparison to the liquefaction susceptibly distribution observed during the 2020 Monte Cristo earthquake. I also give a brief comparison between the post-seismic poroelastic stress relaxation following the 2020 Monte

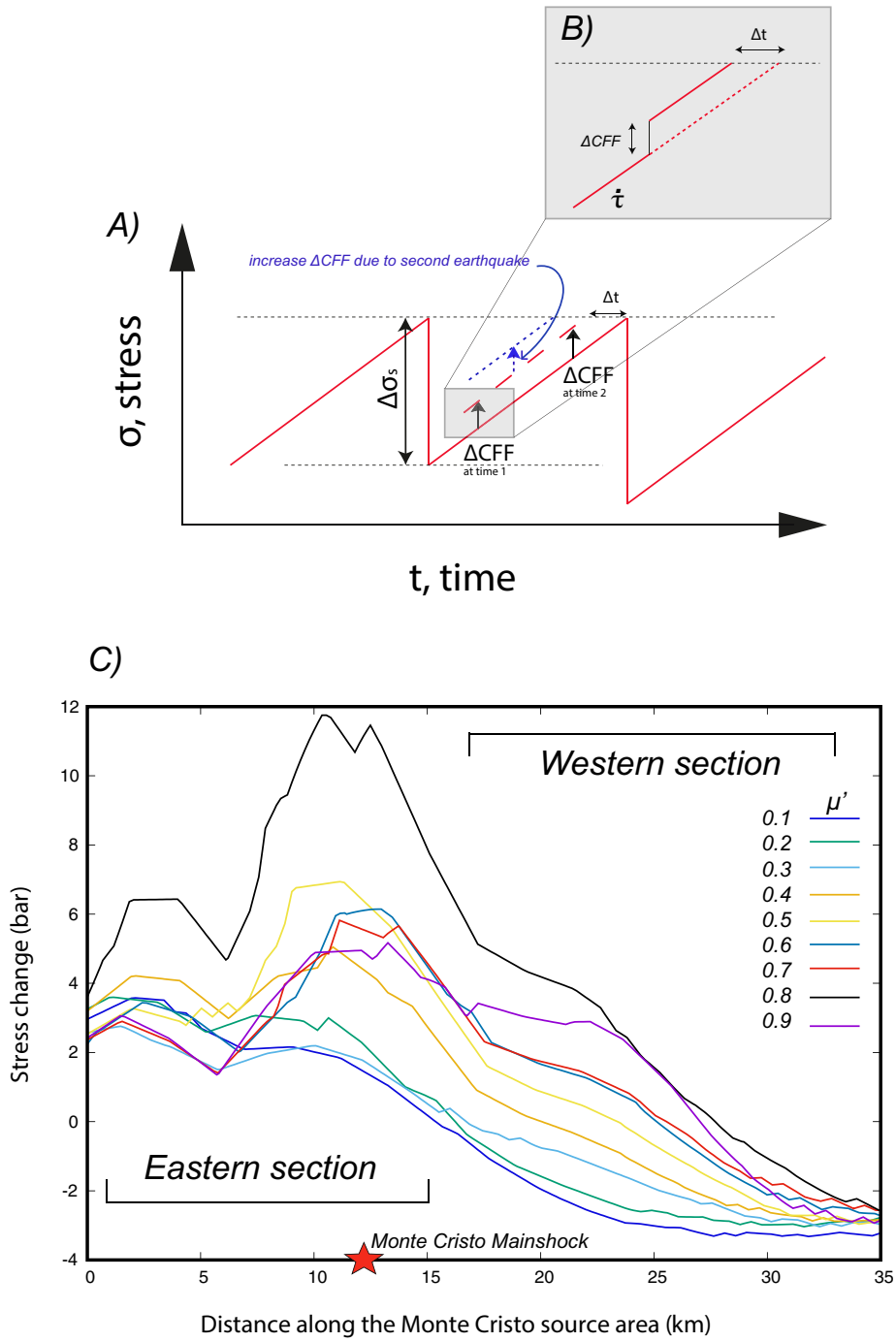

Figure 4. Coulomb stress change, clock time advance, and earthquake periodicity: (a) stress evolution on a fault as a function of the stressing rate $\dot{\tau}$ and the static stress drop $\Delta\sigma_s$. An incremental stress change ΔCFF due to the fault interaction during the earthquake cycle will alter the occurrence of the next large earthquake by causing the clock time advance shift Δt on the stress cycle of the fault (the figure is modified from the original view of Scholz, 2019). (b) Equivalent clock time advance Δt induced by earthquakes at different stages of their stress cycle. (c) Cumulative ΔCFF caused by the 1932 Cedar Mountain and the 1934 Excelsior Mountain earthquakes on the source faults of the Monte Cristo earthquake for various values of the effective friction coefficient. The stress change computation is made by considering the isotropic poroelastic model (Equations 2 and 3). The values on each curve represent the maximum ΔCFF values obtained at ~half of the seismogenic zone. The location of the eastern and western sections of the Monte Cristo earthquake rupture is represented with respect to the surface ruptures and damage zones deduced from field investigations and seismological analysis (Koehler et al., 2021; Ruhl et al., 2021). The red star marks the 2020 Monte Cristo earthquake epicenter. The variation in effective friction coefficient represents a variation in pore pressure regimes at depth (see Equation 2 in Section 3.1).

19449194, 2022, 3, Downloaded from https://agupubs.onlinelibrary.wiley.com/doi/10.1029/2020TC006506 by Portail BibCNRS INSU, Wiley Online Library on [21/02/2024]. See the Terms and Conditions (https://onlinelibrary.wiley.com/terms-and-conditions) on Wiley Online Library for rules of use; OA articles are governed by the applicable Creative Commons License

19449194, 2022, 3, Downloaded from https://agupubs.onlinelibrary.wiley.com/doi/10.1029/2020TC006506 by Portail BibCNRS INSU, Wiley Online Library on [21/02/2024]. See the Terms and Conditions (https://onlinelibrary.wiley.com/terms-and-conditions) on Wiley Online Library for rules of use; OA articles are governed by the applicable Creative Commons License

Cristo earthquake and the early post-seismic deformation distribution associated with the 2019 Ridgecrest, CA earthquake sequence. Finally, I describe in detail the effect of fluid redistribution following the 2020 Monte Cristo earthquake taking into account different geometries of conjugate receiver faults and discuss implications to seismic hazards along Central and Southern Walker Lane faults.

Based on the volumetric strain release following an earthquake and the linear theory of poroelasticity (Rice & Cleary, 1976), modeling the pore pressure change caused by the 2020 Monte Cristo mainshock suggests a correlation between increased pore pressure and the spatial distribution of related aftershocks (Figure 5; Figures S3 and S4 in Supporting Information S1). According to the definition of effective stress (Skempton, 1984), the pore pressure tends to diminishes the normal stress acting on that fault and may create a slip-instability that favors the occurrence of aftershocks.

Figure 5 shows that the pore pressure change caused by Monte Cristo earthquake (Table 1) is in good agreement with the positions of distributed surface shear and extensional cracking near the epicentral area as mapped during the GEER reconnaissance (GEER, 2021) and the USGS liquefaction susceptibility estimate using the liquefaction hazard model of Zhu et al. (2017). The spatial distribution of liquefaction surface features in the Columbus Salt region seems to be consistent with the 5%–20% probability of liquefaction as predicted by the liquefaction hazard map and the spatial distribution of pore pressure change related to the undrained phase of the earthquake (see inset in the Figure 5 and Figure S3 in Supporting Information S1).

Based on laboratory experimental results (Wang, 2007) and the spatial distribution of pore pressure changes (Figure 5 and Figure S3 in Supporting Information S1), the occurrence of the liquefaction-induced lateral spread in the near field appears to be due to the pore pressure build-up during the mainshock causing a decrease in the weight-carrying capacity of the young sedimentary deposits. The positions of the diffuse zones of deformation, the shallow groundwater table, the silt layers approaching the playa margin, the circular pattern of the observed settlements in the Columbus Salt (GEER, 2021), and the modeled elevated pore pressure at depth (Figure 5; Figures S3 and S4 in Supporting Information S1) suggests that the induced liquefaction phenomenon is apparently controlled by a fluidization mechanism of silty sand deposits. Also, the liquefaction process based on a weakening mechanism as described here is consistent with the evolution of sediment specimens from dry to wet during cyclic shearing experiments (Seed & Lee, 1966).

The identification of the liquefaction-induced lateral spread features indicates the presence of low-density sediments deposited in a low-energy environment (GEER, 2021). Indeed: (a) the pore-pressure change modeling based on the volumetric strain release, (b) the laboratory results on sediment specimens, and (c) the geological field observations in the area of the Monte Cristo earthquake testifies that the energy release necessary to induce the liquefaction in the playa margin is highly coupled to the low relative density of sediment and the pore-pressure increase during the co-seismic phase of the earthquake. The coseismic triggered liquefaction processes induced by the 2020 Monte Cristo earthquake includes: sand boils with eruptions of sediments, extensive fractures, and lateral spreading features. These features are similar to those observed in the Salt Wells Valley during the 2019 Ridgecrest sequence (Zimmaro et al., 2020) and in the Wildlife Reserve Array during the 1987 Superstition Hills sequence (Holzer et al., 1989). However, the large distance between the Wildlife Reserve Array and the epicenter of the Mw 6.6 Superstitions Hills earthquake and the maximum values of excess pore water pressure recorded out the maximum amplitude of ground shaking may require an additional pore pressure change due to the fluid diffusion just after the earthquake shaking (Holzer & Youd., 2007; Wang & Manga., 2010).

Note that the USGS real time liquefaction susceptibility map as represented in the inset of the Figure 5 is derived from: (a) peak ground velocity (PGV) data from USGS ShakeMap (Worden & Wald, 2016), (b) topographic slope-derived shear wave velocity over top 30 m (V_{S30}) modeling using the methods of Wald and Allen (2007), and (c) table water depth estimation adapted from the model of Fan et al. (2013). The USGS hazard liquefaction map is presented here as a probabilistic contour map where the predicted land area affected by liquefaction is estimated by percentage within a grid node of [500 × 500] m.

Figures 6a and 6b shows a comparison between the 2019 Ridgecrest and the 2020 Monte Cristo earthquake sequences in terms of poroelastic stress redistribution. The poroelastic stress change modeling is obtained by using an elastic solution and accounts for the temporal variation of Poisson ratios from the undrained to the drained state of fluids. The stress change modeling is performed using extreme values of drained ($\upsilon = 0.15$) and undrained Poisson ratios ($\upsilon_u = 0.31$). These values correspond to high variability in rock rheology before and after

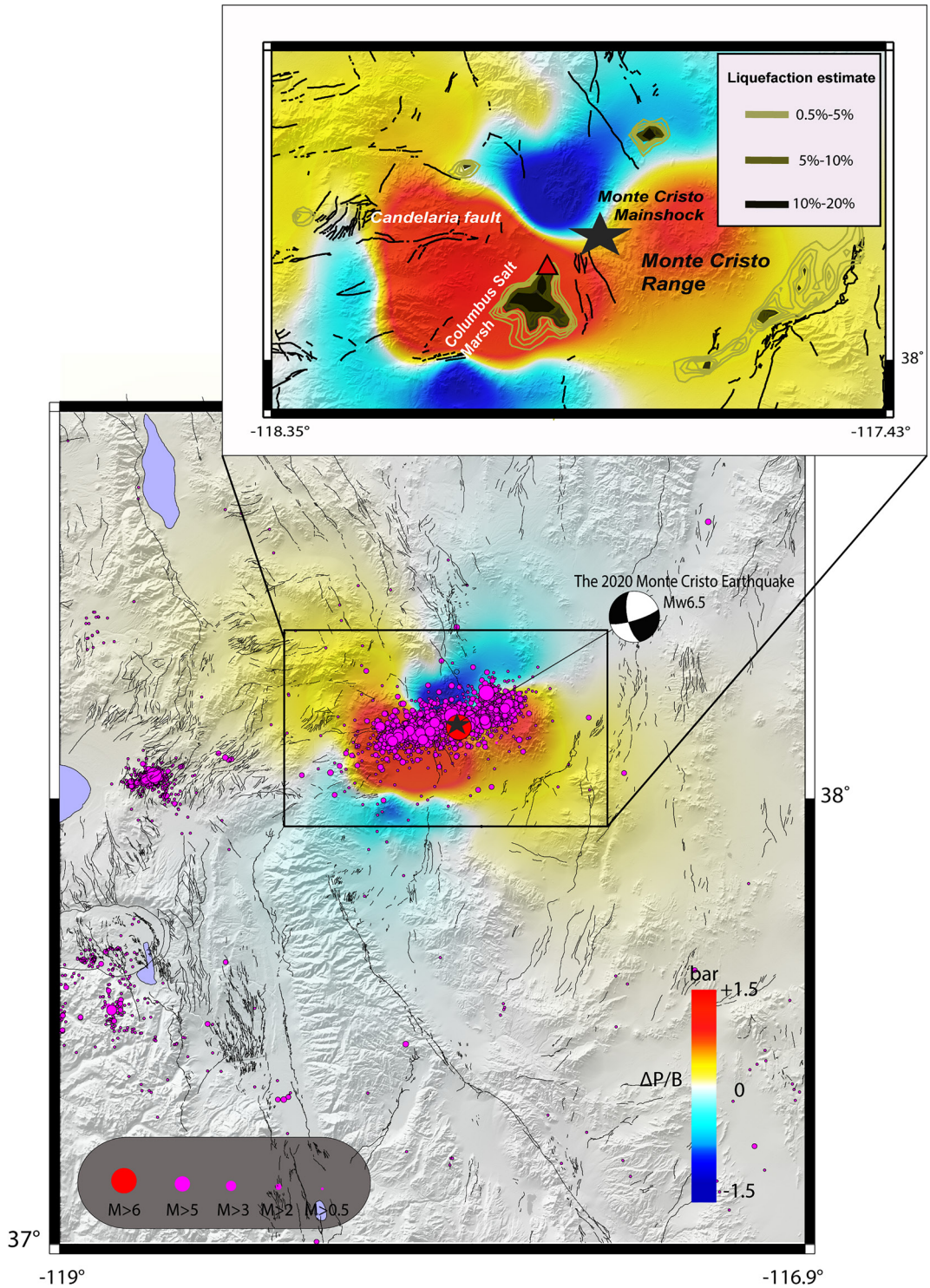

Figure 5. Calculated pore pressure change following the 2020 MC earthquake based on volumetric strain and a theory of linear poroelasticity (Rice & Cleary, 1976). The 2020 coseismic slip creates a high local pore pressure zone that favors the occurrence of the aftershocks sequence (colored magenta circles). According to the Terzaghi definition of effective stress, the increase in pore pressure reduces the normal stress acting on faults and promotes failure. The inset figure represents the relative position of the observed settlements at the ground surface and the location of maximum liquefaction susceptibility following the 2020 Monte Cristo earthquake (red triangle and dark green iso-values respectively). The topography data are from SRTM 15+ (Tozer et al., 2019).

19449194, 2022, 3, Downloaded from https://agupubs.onlinelibrary.wiley.com/doi/10.1029/2020TC006506 by Portail BibCNRS INSU, Wiley Online Library on [21/02/2024]. See the Terms and Conditions (https://onlinelibrary.wiley.com/terms-and-conditions) on Wiley Online Library for rules of use; OA articles are governed by the applicable Creative Commons License

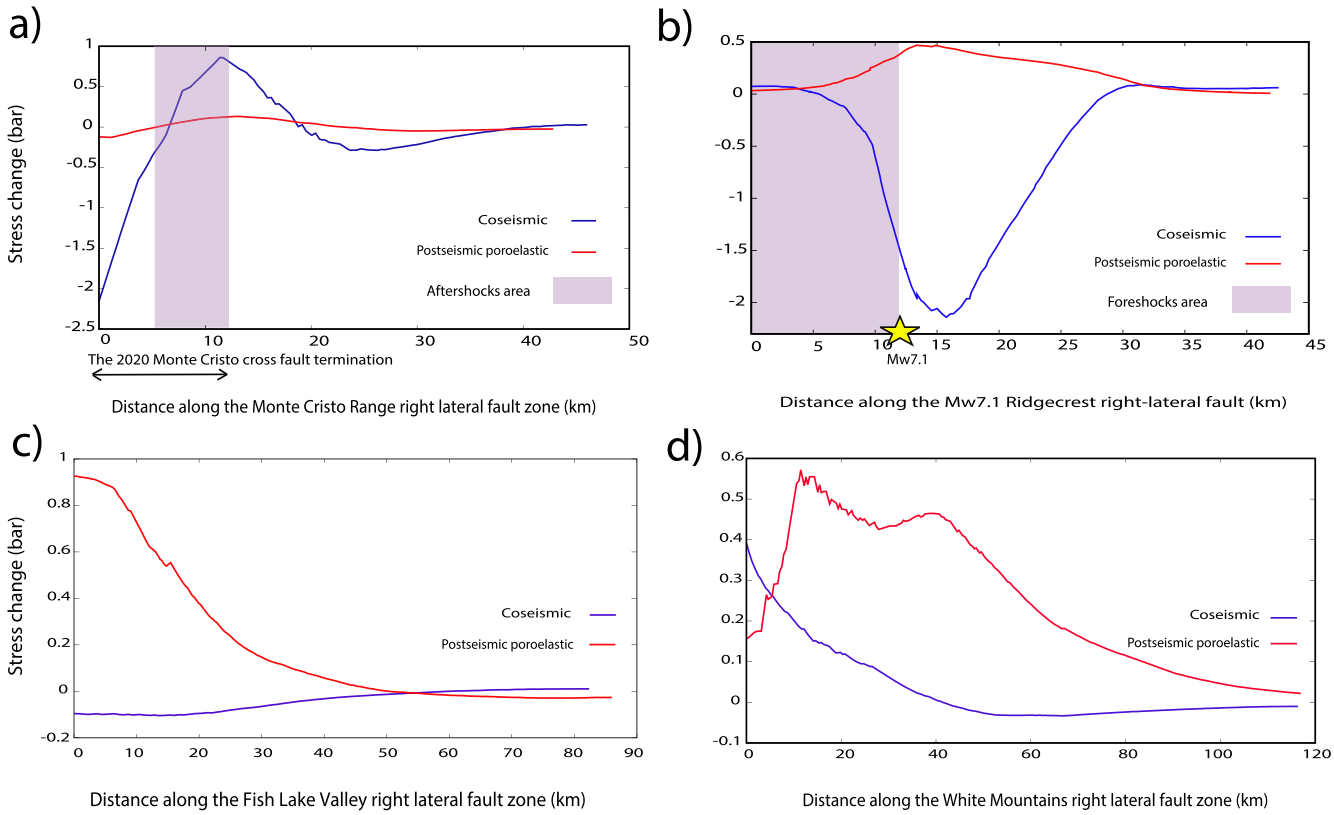

Figure 6. Comparison between the static stress change (in blue) and the poroelastic stress change modeling including the undrained and drained phase of fluids (in red): (a) Poroelastic relaxation caused by the Mw 6.5 Monte Cristo earthquake on nearby right-lateral fixed fault ruptures with strike/dip/rake = 157°/82°/167°, (b) Cumulative stress change caused by the poroelastic relaxation of the Mw 6.4 left-lateral Ridgecrest earthquake on conjugated fixed receiver fault planes with strike/dip/rake = 143°/85°/-165°. (c) Short-term coupled poroelastic stress response due to the 2020 Monte Cristo earthquake along the Fish Lake Valley conjugate fault. The average Fish Lake fault geometry is fixed at strike/dip/rake = 334°/80°/167°. (d) Short-term coupled poroelastic stress response due to the 2020 Monte Cristo earthquake along the White Mountains conjugate fault. The average White Mountains fault geometry is fixed at strike/dip/rake = 171°/80°/165°. The undrained υ_u and drained υ Poisson ratio is fixed at 0.31 and 0.15 respectively. The coseismic stress change is performed using Equations 1 and 3 (see Section 3.1). The short-term poroelastic stress values were obtained using Equation 4 (see Section 3.2). The stress values due to the full poroelastic relaxation are obtained using the methodology described in Section 3.3. The shear and normal stress change values are derived from the coseismic dislocation of each earthquake using the Coulomb 3.3 software (Toda et al., 2011). The pore pressure contribution is added taking into account the variation in rock rheology from the undrained to the drained state of the fluid. The stress change modeling is performed at 8 km depth.

each seismic event and also correspond to the presence of a high density of pre-existing fractures in water-saturated rocks. Note that these values may be not valid for unconsolidated sediments volume with a low fractures density network. The poroelastic stress change modeling in Figure 6b shows a correlation between: (a) the fluid redistribution following the Mw 6.4 left-lateral Ridgecrest earthquake, (b) the stress increase on conjugate fault plane and (c) the occurrence of the Mw 7.1 right-lateral earthquake that occurred 33 hr after the Mw 6.4 event. Based on adapted solutions of poroelasticity, the average value of fluid diffusivity necessary to trigger the Mw 7.1 Ridgecrest is estimated to $\leq 2.32\ 10^4$ cm^2/s (Figure S5 in Supporting Information S1). This value seems to be low compared to the value obtained by Hudnut et al. (1989) for the 1987 Superstition Hills earthquake sequence and related conjugate ruptures and may explain the difference in the time delay between the two sequences (~11 hr for the Superstition Hills earthquakes and ~34 hr for the Ridgecrest earthquakes). Considering the hypothesis that the earthquake triggering process is assisted by fluid migration, the fully poroelastic stress relaxation caused by the 2020 Monte Cristo earthquake (Mw 6.5) shows negative ΔCFF values on nearby target conjugate strike-slip faults situated east of the Mw 6.5 Monte Cristo epicentral area (Figure 6a). The decrease in stress change values from undrained to the drained state of fluids as shown in Figure 6a corresponds to the decrease in the value of pore pressure change at hypocentral depths. Comparing between the Mw 6.5 Monte Cristo sequence and the Mw 6.4 Ridgecrest foreshock sequence (Figures 6a and 6b), the decrease in stress change values from the undrained to the drained fluids-state on faults conjugate to the Monte Cristo earthquake show a remarkable similarity with

19449194, 2022, 3, Downloaded from https://agupubs.onlinelibrary.wiley.com/doi/10.1029/2020TC006506 by Portail BibCNRS INSU, Wiley Online Library on [21/02/2024]. See the Terms and Conditions (https://onlinelibrary.wiley.com/terms-and-conditions) on Wiley Online Library for rules of use; OA articles are governed by the applicable Creative Commons License

the low level of seismicity observed on the right-lateral section of the Monte Cristo rupture (Figure 6a and Figure S6 in Supporting Information S1). For the 2019 Ridgecrest earthquake sequence, the increase in stress changes due to the fluid redistribution following the Mw 6.4 Ridgecrest earthquake seems to follow the high level of earthquake productivity along the conjugate right-lateral rupture plane during the ~30 hr preceding the Mw 7.1 Ridgecrest earthquake (Figure 6b; Figure S5 and S6 in Supporting Information S1).

Considering the poroelastic stress change modeling results, the variation in pore fluid pressure suggests that the fluid migration along conjugate active faults may, in part, control the size of the ruptures. The stress change modeling results (Figure 6b; Figure S5 in Supporting Information S1) and the Spatio-temporal evolution of seismicity along major right-lateral fault planes (Figures S5 and S6 in Supporting Information S1) show that the seismicity rate change is strongly influenced by the post-seismic stress redistribution following the Mw 6.4 Ridgecrest earthquake and the related pore-fluid pressure variations rather than the coseismic stress change. For the 2020 Monte Cristo earthquake sequence, the temporal evolution of seismicity on the eastern (conjugated) section of the fault that follows the Mw 6.5 mainshock (Figure S6 in Supporting Information S1) seems to match with the coseismic level of the stress as modeled by the Coulomb failure criterion (Figure 6a). These results may partially explain the non-occurrence of a second strong earthquake along the conjugate faults close to the Monte Cristo rupture.

In contrast to the stress response along east-west left-lateral faults within the Mina Deflection (Figure 6a) and based on the coupled poroelastic stress solution as seen in Equation 4, the short-term coupled poroelastic stress change caused by the 2020 Monte Cristo earthquake on the conjugate Fish Lake Valley and White Mountains fault zones shows a significant increase in stress magnitude when the pore fluid diffusion process is taken into account in the Coulomb stress modeling (Figures 6c and 6d). The temporal variation from negative to positive ΔCFF value as represented by the anti-correlated curves in Figure 6 reveals that the increase in pore pressure due to the fluid migration may promote earthquakes on receiver faults in some places where the coseismic stress change modeling predicts an absence of earthquake activity.

Considering the post-seismic stress redistribution due to the fluid diffusion and an average strain rate of 40–50 nanostrain/yr for the Southern Walker Lane (Kreemer et al., 2009), the 0.5–0.8 bar stress loading on target conjugate faults suggests that the White Mountains and Fish Lake Valley fault zones are under an average earthquake clock time advance of 50 and 80 years, respectively. Based on an average return period of ~250 years for large earthquakes within the Walker Lane determined by seismicity analyses (Ryall & Priestley, 1975) and the poroelastic stress loading values obtained by the Coulomb stress modeling presented in this paper (Figures 6c and 6d), the stress changes from regional earthquakes have advanced the timing of the next large earthquake on the White Mountains and Fish Lake Valley faults by several decades.

The earthquake return period of ~250 years deduced from seismology is comparable to the recurrence time of an earthquake with a magnitude of $M \sim 6.7$ estimated from 14 ± 5 m offset alluvial fan deposits along the north-northwestern part of the White Mountains fault zone (Lifton et al., 2021). The geological recurrence interval is estimated using the ratio between coseismic displacement and geological slip rate along the selected faults. First, the 14 ± 5 m multiple events offsets are combined with a Fan exposure age estimate of 7.3 + 4.2/-4.5 kyr deduced from geochronological analysis (Lifton et al., 2021). Based on these values, a minimum geological slip rate of ~1 mm/yr for the White Mountains fault zone is estimated (Lifton et al., 2021). Second, I add a slip rate of 1.9 mm/yr to the ~1 mm/yr slip rate because a part of the dextral shear on the Owens Valley is essentially partitioned into the White Mountain fault zone (DeLano et al., 2019). Based on these considerations, a newly geological slip rate of ~2.9 mm/yr is assumed for the right-lateral White Mountains fault zone. Comparing the ~2.9 mm/yr slip rate with a displacement of ~0.6 m for a single event along ~50 km-long Holocene NNW-SSE trending dextral faults and ~15 km-long fault widths, an average recurrence time of ~210 years for an event with $M \sim 6.7$ is determined for the White Mountains fault zone.

For an average co-seismic displacement of 1.8 m and using the same considerations, a recurrence time interval of ~620 years is expected for an earthquake with Mw ~7.1 along the White Mountains fault zone. In this case, the clock time advance will represent a shift of 8% of the total recurrence time interval for an event with magnitude Mw ~7.1. Considering the same approach with introducing a geological slip rate of ~3.3 mm/yr (Wesnousky, 2005), the Fish Lake Valley fault zone would produce a recurrence time interval of ~545 years for a

19449194, 2022, 3, Downloaded from https://agupubs.onlinelibrary.wiley.com/doi/10.1029/2020TC006506 by Portail BibCNRS INSU, Wiley Online Library on [21/02/2024]. See the Terms and Conditions (https://onlinelibrary.wiley.com/terms-and-conditions) on Wiley Online Library for rules of use; OA articles are governed by the applicable Creative Commons License

similar earthquake-size. Here, the fault interaction and the fluid redistribution will influence the earthquake cycle by a shift of more than 14% of the total recurrence time interval.

The earthquake recurrence interval of large earthquakes expected for a Fish Lake Valley and the White Mountains fault zones is low compared to the 1600–2300 years recurrence time interval obtained for right-lateral structures in Mina Deflection (Angster et al., 2019). This may reflect a large-scale fault interaction and may indicate that the Fish Lake Valley and the White Mountains faults are in an advanced stage of their seismic cycles. Considering the Coulomb stress change modeling as proposed in this paper, the Coulomb stress values may reflect the contribution of both fault interaction and related fluid migration to the earthquake cycle for major dextral faults on Southern Walker Lane. Note that the large variations in the earthquake recurrence time intervals may also related to the large variation in the slip rates along individual faults.

6. Conclusions

In May 2020, an earthquake sequence with magnitude Mw 6.5 struck the Central Walker Lane. The focal solutions combined with the InSAR and GPS data, as well as field observations (GEER, 2021; Koehler et al., 2021) show a complex conjugate fault slip distribution. Based on our estimation of fault rupture parameters, a stress change modeling of historical events suggests fault interactions between the three major earthquakes within the Central Walker Lane: the 1932 Cedar Mountain earthquake (Mw 7.1), the 1934 Excelsior Mountain earthquake (Mw 6.5), and the 2020 Monte Cristo (Mw 6.5) earthquake. Following the 1932 Cedar Mountain earthquake, the static stress increased from 0.2 to 2 bars on the Excelsior Mountain and Monte Cristo Range *en echelon* left-lateral fault systems. Considering the average strain rate of 35 nanostrain yr^{-1} across the Mina Deflection, the stress redistribution following the 1932 Cedar Mountain earthquake may have increased the earthquake occurrence time on nearby *en echelon* left-lateral faults systems from 20 to 230 years. The computed clock time advance imparted by the 1932 Cedar Mountain earthquake (Mw 7.1) on conjugate fault planes added to a tectonic loading of 32–65 nanostrain yr^{-1} may partly explain the 2–88 years earthquakes time delays on Central Walker Lane earthquakes.

Despite the similarities in fault interaction with others conjugate triggering mechanisms (Hudnut et al., 1989; Kariche et al., 2018), the static stress change modeling using an isotropic poroelastic model shows no correlation between the fluid redistribution caused by large right-lateral ruptures and the occurrence of moderate to strong earthquakes on conjugated *en echelon* left-lateral faults. Compared to several case studies of conjugate triggering mechanisms (Fialko, 2004; Kariche et al., 2018, 2019; Shi & Wei, 2020), the 'no apparent' fluid redistribution effect may also explain the large time delay between the Cedar Mountain and Monte Cristo earthquakes (~88 years). Among the main historical and recent earthquakes, the static stress change modeling at half of the seismogenic depth shows that the 1932 Cedar Mountain earthquake (Mw 7.1) significantly influenced the stress field in Central Walker Lane.

The structural characteristics of tectonic blocks limited by active and seismogenic faults with *en echelon* fault geometry provide the patterns of earthquake stress transfer as for the case of a simple pure shear deformation applied to oblique plate convergence (Kariche et al., 2017). In addition to other tectonic patterns, the remaining question in Central Walker Lane is the role of fluid migration following the occurrence of large earthquakes. Using different values of the effective friction coefficient, the effect of the stress change modeling of the Mw 7.1 Cedar Mountain earthquake on conjugate left-lateral strike-slip faults shows a stress proportionality with the increase in the effective friction coefficient. Similar results are also obtained considering more complex crustal rheologies with a comparable ΔCFF loading reaching 2–5 bar covering the 2020 Monte Cristo epicentral area. The coupled poroelastic stress change response caused by the 2020 Monte Cristo earthquake on the right-lateral Fish Lake Valley and White Mountains fault zones shows an intermediate increase in stress change considering both the undrained and drained phase of fluids. The pore pressure change modeling using the linear theory of poroelasticity shows a causative relation between the spatial distribution of aftershocks following the 2020 Monte Cristo earthquake and the increase in pore-fluid pressure. From a structural point of view, fluid migration may occur on nearby subsidiary normal fractures related to diffuse continental extension from the Mina Deflection to the Southern Walker Lane. This complex mode of stress redistribution implies that the reactivation of large active strike slip faults in the Central Walker Lane require a high coefficient of friction ($\mu > 0.6$) and a fluid migration process along active faults in the Southern Walker Lane domain. The result of stress change under pore-fluid stimulus has the potential to complement geologic, geodetic, and seismic data in seismic hazard assessment.

19449194, 2022, 3, Downloaded from https://agupubs.onlinelibrary.wiley.com/doi/10.1029/2020TC006506 by Portail BibCNRS INSU, Wiley Online Library on [21/02/2024]. See the Terms and Conditions (https://onlinelibrary.wiley.com/terms-and-conditions) on Wiley Online Library for rules of use; OA articles are governed by the applicable Creative Commons License

Data Availability Statement

Coseismic GPS offsets data are from MAGNET/UNAVCO-NOTA real time data solutions (Blewitt et al., 2018) and were downloaded at the Nevada Geodetic Laboratory website (http://geodesy.unr.edu/magnet.php, last updated data 19/06/2020). The surface rupture data are from the University of Nevada, Reno and was downloaded in the original form at http://www.nbmg.unr.edu/Geohazards/Earthquakes/MonteCristoRangeEQData.html. The seismicity data are from the Northern California Earthquake Catalog and were downloaded at https://ncedc.org/ncedc/catalog-search.html. The earthquake focal mechanisms were obtained through Saint Louis University available at (http://www.eas.slu.edu/eqc/eqc_mt/MECH.NA/). The author thanks Ross Stein (USGS, Menlo Park) and Shinji Toda (Sendai University) for sharing the Coulomb 3.3 software. The Sentinel-1A SAR data were downloaded from ESA Copernicus program (https://scihub.copernicus.eu/). The line-of-sight (LOS) displacements data are available through https://zenodo.org/record/4671183#.YRkGq986-Ul.

Acknowledgments
The author thanks M. Meghraoui (IPG Strasbourg), R. Toussaint (IPG Strasbourg), and R. W Simpson (ex. USGS California) for discussions on the conceptual framework of stress transfer and poroelastic deformation. The author gratefully thanks Rich D. Koehler (University of Nevada, Reno) and A. Hatem (USGS) who kindly reviewed the earlier version of the manuscript and provide valuable suggestions and comments. The author also thanks to the Associate Editor and P. M Figueiredo (North Carolina State University) for their comments and suggestions on the article. This research program was funded by the Direction of Research at MESRS and the Direction Europe de la Recherche et Coopération Internationale (DERCI-CNRS). Some figures were prepared using the public domain Generic Mapping Tools (GMT) software (Wessel & Smith, 1998).

References

Angster, S. J., Wesnousky, S. G., Figueiredo, P. M., Owen, L. A., & Hammer, S. J. (2019). Late Quaternary slip rates for faults of the central Walker Lane (Nevada, USA): Spatiotemporal strain release in a strike-slip fault system. *Geosphere*, *15*(5), 1460–1478. https://doi.org/10.1130/ges02088.1

Beeler, N., Simpson, R., Hickman, S., & Lockner, D. (2000). Pore fluid pressure, apparent friction, and Coulomb failure. *Journal of Geophysical Research*, *105*(B11), 25533–25542. https://doi.org/10.1029/2000jb900119

Bell, J. W., dePolo, C. M., Ramelli, A. R., Sarna-Wojcicki, A. M., & Meyer, C. (1999). Surface faulting and paleoseismic history of the 1932 Cedar Mountain earthquake area, west-central Nevada, and implications for modern tectonics of the Walker Lane. *Geological Society of America Bulletin*, *111*(6), 791–807. https://doi.org/10.1130/0016-7606(1999)111<0791:sfapho>2.3.co;2

Bennett, R., Wernicke, B., Niemi, N., Friedrich, A., & Davis, J. (2003). Contemporary strain rates in the northern Basin and Range province from GPS data. *Tectonics*, *22*(2). https://doi.org/10.1029/2001tc001355

Biot, M. A., & Willis, D. (1957). The elastic coefficients of the theory of consolidation. *Journal of Applied Mechanics*, *24*, 594–601. https://doi.org/10.1115/1.4011606

Blewitt, G., Hammond, W., & Kreemer, C. (2018). Harnessing the GPS data explosion for interdisciplinary science. *Eos*, *99*. https://doi.org/10.1029/2018EO104623

Bormann, J. M., Hammond, W. C., Kreemer, C., & Blewitt, G. (2016). Accommodation of missing shear strain in the Central Walker Lane, western North America: Constraints from dense GPS measurements. *Earth and Planetary Science Letters*, *440*, 169–177. https://doi.org/10.1016/j.epsl.2016.01.015

Bormann, J. M., Morton, E. A., Smith, K. D., Kent, G. M., Honjas, W. S., Plank, G. L., & Williams, M. C. (2021). Nevada Seismological Laboratory rapid seismic monitoring deployment and data availability for the 2020 M ww 6.5 Monte Cristo Range, Nevada, earthquake sequence. *Seismological Society of America*, *92*(2A), 810–822. https://doi.org/10.1785/0220200344

Bosl, W., & Nur, A. (2002). Aftershocks and pore fluid diffusion following the 1992 Landers earthquake. *Journal of Geophysical Research*, *107*(B12). https://doi.org/10.1029/2001jb000155

Carlson, C. W., Pluhar, C. J., Glen, J. M., & Farner, M. J. (2013). Kinematics of the west-central Walker Lane: Spatially and temporally variable rotations evident in the Late Miocene Stanislaus Group. *Geosphere*, *9*(6), 1530–1551. https://doi.org/10.1130/ges00955.1

Chambon, G., & Rudnicki, J. W. (2001). Effects of normal stress variations on frictional stability of a fluid-infiltrated fault. *Journal of Geophysical Research*, *106*(B6), 11353–11372. https://doi.org/10.1029/2001jb900002

Dee, S., Koehler, R. D., Elliott, A. J., Hatem, A. E., Pickering, A., Pierce, I., et al. (2021). *Surface rupture map of the 2020 M 6.5 Monte Cristo range earthquake, Esmeralda and Mineral counties, Nevada*. University of Nevada.

DeLano, K., Lee, J., Roper, R., & Calvert, A. (2019). Dextral, normal, and sinistral faulting across the eastern California shear zone–Mina deflection transition, California-Nevada, USA. *Geosphere*, *15*(4), 1206–1239. https://doi.org/10.1130/ges01636.1

Doser, D. I. (1988). Source parameters of earthquakes in the Nevada seismic zone, 1915–1943. *Journal of Geophysical Research*, *93*(B12), 15001–15015. https://doi.org/10.1029/jb093ib12p15001

Fan, Y., Li, H., & Miguez-Macho, G. (2013). Global patterns of groundwater table depth. *Science*, *339*(6122), 940–943. https://doi.org/10.1126/science.1229881

Faulds, J. E., Henry, C. D., & Hinz, N. H. (2005). Kinematics of the northern Walker Lane: An incipient transform fault along the Pacific–North American plate boundary. *Geology*, *33*(6), 505–508. https://doi.org/10.1130/g21274.1

Fialko, Y. (2004). Evidence of fluid-filled upper crust from observations of postseismic deformation due to the 1992 Mw7. 3 Landers earthquake. *Journal of Geophysical Research*, *109*(B8). https://doi.org/10.1029/2004jb002985

GEER. (2021). Nevada 2020 Earthquake GEER Report. [Data set]. GEER. https://doi.org/10.18118/G67H4F

Hammond, W. C., Blewitt, G., Kreemer, C., Koehler, R. D., & Dee, S. (2021). Geodetic observation of seismic cycles before, during, and after the 2020 Monte Cristo Range, Nevada earthquake. *Seismological Society of America*, *92*(2A), 647–662. https://doi.org/10.1785/0220200338

Holzer, T., Hanks, T., & Youd, T. (1989). Dynamics of liquefaction during the 1987 Superstition Hills, California, earthquake. *Science*, *244*(4900), 56–59. https://doi.org/10.1126/science.244.4900.56

Holzer, T. L., & Youd, T. L. (2007). Liquefaction, ground oscillation, and soil deformation at the Wildlife Array, California. *Bulletin of the Seismological Society of America*, *97*(3), 961–976. https://doi.org/10.1785/0120060156

Hudnut, K. W., Seeber, L., & Pacheco, J. (1989). Cross-fault triggering in the November 1987 Superstition Hills earthquake sequence, southern California. *Geophysical Research Letters*, *16*(2), 199–202. https://doi.org/10.1029/gl016i002p00199

Jackson, J., & Molnar, P. (1990). Active faulting and block rotations in the western Transverse Ranges, California. *Journal of Geophysical Research*, *95*(B13), 22073–22087. https://doi.org/10.1029/jb095ib13p22073

Kariche, J., Meghraoui, M., Ayadi, A., & Boughacha, M. (2017). Stress change and fault interaction from a two century-long earthquake sequence in the Central Tell Atlas, Algeria. *Bulletin of the Seismological Society of America*, *107*(6), 2624–2635. https://doi.org/10.1785/0120170041

19449194, 2022, 3, Downloaded from https://agupubs.onlinelibrary.wiley.com/doi/10.1029/2020TC006506 by Portail BibCNRS INSU, Wiley Online Library on [21/02/2024]. See the Terms and Conditions (https://onlinelibrary.wiley.com/terms-and-conditions) on Wiley Online Library for rules of use; OA articles are governed by the applicable Creative Commons License

Kariche, J., Meghraoui, M., Timoulali, Y., Cetin, E., & Toussaint, R. (2018). The Al Hoceima earthquake sequence of 1994, 2004 and 2016: Stress transfer and poroelasticity in the Rif and Alboran Sea region. *Geophysical Journal International*, *212*(1), 42–53. https://doi.org/10.1093/gji/ggx385

Kariche, J., Meghraoui, M., & Toussaint, R. (2019). Stress transfer and poroelasticity associated to the 2019 Ridgecrest (California) earthquake sequences. In *AGU Fall Meeting Abstracts* (pp. S31G–0505).

Koehler, R. D., Dee, S., Elliott, A., Hatem, A., Pickering, A., Pierce, I., & Seitz, G. (2021). Field response and surface-rupture characteristics of the 2020 M 6.5 Monte Cristo Range Earthquake, Central Walker Lane, Nevada. *Seismological Society of America*, *92*(2A), 823–839. https://doi.org/10.1785/0220200371

Kreemer, C., Blewitt, G., Hammond, W. C., Oldow, J., & Cashman, P. (2009). Geodetic constraints on contemporary deformation in the northern Walker Lane: 2. Velocity and strain rate tensor analysis. In *Late cenozoic structure and evolution of the Great Basin–Sierra Nevada Transition* (Vol. 447, pp. 17–31). Geological Society of America Special Paper. https://doi.org/10.1130/2009.2447(02)

Kreemer, C., Blewitt, G., & Klein, E. C. (2014). A geodetic plate motion and Global Strain Rate Model. *Geochemistry, Geophysics, Geosystems*, *15*(10), 3849–3889. https://doi.org/10.1002/2014gc005407

Lee, J., Garwood, J., Stockli, D. F., & Gosse, J. (2009). Quaternary faulting in Queen Valley, California-Nevada: Implications for kinematics of fault-slip transfer in the eastern California shear zone–Walker Lane belt. *Geological Society of America Bulletin*, *121*(3–4), 599–614. https://doi.org/10.1130/b26352.1

Li, B., Li, Y., Jiang, W., Su, Z., & Shen, W. (2020). Conjugate ruptures and seismotectonic implications of the 2019 Mindanao earthquake sequence inferred from Sentinel-1 InSAR data. *International Journal of Applied Earth Observation and Geoinformation*, *90*, 102127. https://doi.org/10.1016/j.jag.2020.102127

Lifton, Z. M., Lee, J., Frankel, K. L., Newman, A. V., & Schroeder, J. M. (2021). Quaternary slip rates on the White Mountains fault zone, eastern California: Implications for comparing geologic to geodetic slip rates across the Walker Lane. *GSA Bulletin*, *133*(1–2), 307–324. https://doi.org/10.1130/b35332.1

Nagorsen-Rinke, S., Lee, J., & Calvert, A. (2013). Pliocene sinistral slip across the Adobe Hills, eastern California–western Nevada: Kinematics of fault slip transfer across the Mina deflection. *Geosphere*, *9*(1), 37–53. https://doi.org/10.1130/ges00825.1

Nur, A., Ron, H., & Scotti, O. (1986). Fault mechanics and the kinematics of block rotations. *Geology*, *14*(9), 746–749. https://doi.org/10.1130/0091-7613(1986)14<746:FMATKO>2.0.CO;2

Okada, Y. (1992). Internal deformation due to shear and tensile faults in a half-space. *Bulletin of the Seismological Society of America*, *82*(2), 1018–1040. https://doi.org/10.1785/bssa0820021018

Peltzer, G., Rosen, P., Rogez, F., & Hudnut, K. (1998). Poroelastic rebound along the Landers 1992 earthquake surface rupture. *Journal of Geophysical Research*, *103*(B12), 30131–30145. https://doi.org/10.1029/98jb02302

Petronis, M. S., Geissman, J. W., Oldow, J. S., McIntosh, W. C., & Cashman, P. (2009). Late Miocene to Pliocene vertical-axis rotation attending development of the Silver Peak–Lone Mountain displacement transfer zone, west-central Nevada. *Late Cenozoic structure and evolution of the Great Basin–Sierra Nevada transition* (Vol. 447, pp. 215–253). Geological Society of America Special Paper.

Pierce, I. K. D., Wesnousky, S. G., Owen, L. A., Bormann, J. M., Li, X., & Caffee, M. (2021). Accommodation of plate motion in an incipient Strike-Slip System: The Central Walker Lane. *Tectonics*, *40*(2). https://doi.org/10.1029/2019TC005612

Ponti, D. J., Blair, J. L., Rosa, C. M., Thomas, K., Pickering, A. J., Akciz, S., et al. (2020). Documentation of surface fault rupture and ground-deformation features produced by the 4 and 5 July 2019 M w 6.4 and M w 7.1 Ridgecrest Earthquake Sequence. *Seismological Society of America*, *91*(5), 2942–2959. https://doi.org/10.1785/0220190322

Reasenberg, P. A., & Simpson, R. W. (1992). Response of regional seismicity to the static stress change produced by the Loma Prieta earthquake. *Science*, *255*(5052), 1687–1690. https://doi.org/10.1126/science.255.5052.1687

Rice, J. R., & Cleary, M. P. (1976). Some basic stress diffusion solutions for fluid-saturated elastic porous media with compressible constituents. *Reviews of Geophysics*, *14*(2), 227–241. https://doi.org/10.1029/rg014i002p00227

Ruhl, C. J., Morton, E. A., Bormann, J. M., Hatch-Ibarra, R., Ichinose, G., & Smith, K. D. (2021). Complex Fault Geometry of the 2020 M ww 6.5 Monte Cristo Range, Nevada, Earthquake Sequence. *Seismological Society of America*, *92*(3), 1876–1890. https://doi.org/10.1785/0220200345

Ryall, A., & Priestley, K. (1975). Seismicity, secular strain, and maximum magnitude in the Excelsior Mountains area, western Nevada and eastern California. *Geological Society of America Bulletin*, *86*(11), 1585–1592. https://doi.org/10.1130/0016-7606(1975)86<1585:SSSAMM>2.0.CO;2

Scholz, C. H. (2019). *The mechanics of earthquakes and faulting*. Cambridge University Press.

Seed, H. B., & Lee, K. L. (1966). Liquefaction of saturated sands during cyclic loading. *Journal of the Soil Mechanics and Foundations Division*, *92*(6), 105–134. https://doi.org/10.1061/jsfeaq.0000913

Segall, P., & Rice, J. R. (1995). Dilatancy, compaction, and slip instability of a fluid-infiltrated fault. *Journal of Geophysical Research*, *100*(B11), 22155–22171. https://doi.org/10.1029/95jb02403

Shi, Q., & Wei, S. (2020). Highly heterogeneous pore fluid pressure enabled rupture of orthogonal faults during the 2019 Ridgecrest Mw7.0 Earthquake. *Geophysical Research Letters*, *47*, e2020GL089827. https://doi.org/10.1029/2020GL089827

Skempton, A. (1984). Effective stress in soils, concrete and rocks. *Selected papers on soil mechanics*, *1032*, 4–16. https://doi.org/10.1680/sposm.02050.0014

Stein, R. S., Barka, A. A., & Dieterich, J. H. (1997). Progressive failure on the North Anatolian fault since 1939 by earthquake stress triggering. *Geophysical Journal International*, *128*(3), 594–604. https://doi.org/10.1111/j.1365-246x.1997.tb05321.x

Stewart, J. H. (1980). *Geology of Nevada* (Vol. 4, p. 136). Nevada Bureau of Mines and Geology Special Publication.

Thatcher, W., Foulger, G., Julian, B., Svarc, J., Quilty, E., & Bawden, G. (1999). Present-day deformation across the Basin and Range province, western United States. *Science*, *283*(5408), 1714–1718. https://doi.org/10.1126/science.283.5408.1714

Toda, S., Stein, R. S., Sevilgen, V., & Lin, J. (2011). Coulomb 3.3 Graphic-rich deformation and stress-change software for earthquake, tectonic, and volcano research and teaching—User guide. *US Geological Survey open-file report*, *1060*, 63.

Tozer, B., Sandwell, D., Smith, W., Olson, C., Beale, J., & Wessel, P. (2019). Global bathymetry and topography at 15 arc sec: SRTM15+. *Earth and Space Science*, *6*(10), 1847–1864. https://doi.org/10.1029/2019ea000658

Wald, D. J., & Allen, T. I. (2007). Topographic slope as a proxy for seismic site conditions and amplification. *Bulletin of the Seismological Society of America*, *97*(5), 1379–1395. https://doi.org/10.1785/0120060267

Wang, C., & Manga, M. (2010). *Earthquakes and water* (Vol. 114). Springer.

Wang, C.-Y. (2007). Liquefaction beyond the near field. *Seismological Research Letters*, *78*(5), 512–517. https://doi.org/10.1785/gssrl.78.5.512

Wells, D. L., & Coppersmith, K. J. (1994). New empirical relationships among magnitude, rupture length, rupture width, rupture area, and surface displacement. *Bulletin of the Seismological Society of America*, *84*(4), 974–1002.

Wesnousky, S. G. (2005). Active faulting in the Walker Lane. *Tectonics*, *24*(3). https://doi.org/10.1029/2004tc001645

19449194, 2022, 3, Downloaded from https://agupubs.onlinelibrary.wiley.com/doi/10.1029/2020TC006506 by Portail BibCNRS INSU, Wiley Online Library on [21/02/2024]. See the Terms and Conditions (https://onlinelibrary.wiley.com/terms-and-conditions) on Wiley Online Library for rules of use; OA articles are governed by the applicable Creative Commons License

Wessel, P., & Smith, W. H. (1998). New, improved version of Generic Mapping Tools released. *Eos, Transactions American Geophysical Union*, *79*(47), 579. https://doi.org/10.1029/98eo00426

Worden, C., & Wald, D. (2016). *Shake map manual online: Technical manual, user's guide, and software guide* (pp. 1–156). United States Geological Survey.

Yamashita, T., & Tsutsumi, A. (2018). *Involvement of fluids in earthquake ruptures* (Vol. 10, pp. 978–4). Springer.

Zhu, J., Baise, L. G., & Thompson, E. M. (2017). An updated geospatial liquefaction model for global application an updated geospatial liquefaction model for global application. *Bulletin of the Seismological Society of America*, *107*(3), 1365–1385. https://doi.org/10.1785/0120160198

Zimmaro, P., Nweke, C. C., Hernandez, J. L., Hudson, K. S., Hudson, M. B., Ahdi, S. K., et al. (2020). Liquefaction and related ground failure from July 2019 Ridgecrest earthquake sequence. *Bulletin of the Seismological Society of America*, *110*(4), 1549–1566. https://doi.org/10.1785/0120200025

19449194, 2022, 3, Downloaded from https://agupubs.onlinelibrary.wiley.com/doi/10.1029/2020TC006506 by Portail BibCNRS INSU, Wiley Online Library on [21/02/2024]. See the Terms and Conditions (https://onlinelibrary.wiley.com/terms-and-conditions) on Wiley Online Library for rules of use; OA articles are governed by the applicable Creative Commons License